Statistica Sinica **29** (2019), 1253-1276
doi:https://doi.org/10.5705/ss.202017.0475

A TEST FOR ISOTROPY ON A SPHERE USING SPHERICAL HARMONIC FUNCTIONS

Indranil Sahoo[1], Joseph Guinness[2] and Brian J. Reich[1]

[1]*North Carolina State University and* [2]*Cornell University*

Abstract: Analyses of geostatistical data are often based on the assumption that the spatial random field is isotropic. This assumption, if erroneous, can adversely affect model predictions and statistical inferences. Today, many applications consider global data, and hence, it is necessary to check the assumption of isotropy on a sphere. This study proposes a test for spatial isotropy on a sphere. The data are first projected onto the set of spherical harmonic functions. Under isotropy, the spherical harmonic coefficients are uncorrelated, but are correlated if the underlying fields are not isotropic. This motivates a test based on the sample correlation matrix of the spherical harmonic coefficients. In particular, we use the largest eigenvalue of this matrix as the test statistic. Extensive simulations are conducted to assess the Type-I errors of the test under different scenarios. Our method requires temporal replication in the data and, hence, is applicable to many data sets in the Earth sciences. We show how temporal correlation affects the test and provide a method for handling such correlation. We also gauge the power of the test as we move away from isotropy. The method is applied to near-surface air temperature data, which is part of the HadCM3 model output. Although we do not expect global temperature fields to be isotropic, we propose several anisotropic models, with increasing complexity, each of which has an isotropic process as a model component. Then, we apply the test to the isotropic component in a sequence of such models to determine how well the models capture the anisotropy in the fields.

Key words and phrases: Anisotropy, spatial statistics, spherical harmonic representation.

1. Introduction

Modeling spatial dependence is a major challenge when analyzing geostatistical data. It is common to assume that the spatial covariance function is isotropic, meaning that the correlation between observations at any two locations depends only on the distance between those locations, and not on their relative orientation (Guan, Sherman and Calvin (2004)). With advancements in technology, we

now observe massive amounts of data, especially in atmospheric sciences. Satellites and ground-based monitoring stations collect data, and large-scale climatic models produce data covering the entire globe. Thus, it is important to develop methods for analyzing spatial data observed on spheres. Hence, it is necessary to understand the inherent correlation structure of the process on the sphere. Assuming that the process is isotropic leads to simpler interpretation of the correlation structure and reduces the computational complexity. However, in many applications, isotropy may not be a reasonable assumption, leading to erroneous model fitting and predictions.

A common method for checking for isotropy is to compare sample semivariograms for different directions (Cressie (1993)). Many approaches use directional variograms to construct tests with stationary alternatives (Matheron (1961); Diggle (1981); Cabana (1987); Baczkowski and Mardia (1990); Isaaks and Srivastava (2001)). Some nonparametric methods are based on estimates of a variogram or a covariogram (Lu and Zimmerman (2001); Guan, Sherman and Calvin (2004); Maity and Sherman (2012)). The notion of testing for second-order properties using the asymptotic joint normality of a sample variogram evaluated at different spatial lags was established by Lu and Zimmerman (2001). The subsequent works of Guan, Sherman and Calvin (2004) and Maity and Sherman (2012) are based on these ideas. Li, Genton and Sherman (2007, 2008) and Jun and Genton (2012) consider spatiotemporal data and use approaches similar to those of Lu and Zimmerman (2001), Guan, Sherman and Calvin (2004), and Maity and Sherman (2012). Bowman and Crujeiras (2013) give a more computational approach for testing isotropy in spatial data using a robust form of the empirical variogram based on a fourth-root transformation.

Haskard (2007) extends the Matérn correlation to include anisotropy, facilitating a test for isotropy. Fuentes (2007) describes a spectral method based on estimating parameters that govern the directionality in the spatial dependence (anisotropy), using approximate likelihoods. Matsuda and Yajima (2009) consider a generalized Matérn class that allows for anisotropy and construct a likelihood ratio test for isotropy.

The aforementioned methods all apply to random fields on the Euclidean space, $\mathbb{R}^d, d > 1$, and have stationarity as the alternative. However, a sphere differs from the Euclidean space in the sense that there is no agreed upon way to define stationary processes on a sphere, which are not isotropic. Some authors have referred to axially symmetric processes as "stationary" processes on spheres. However, the notion of an axially symmetric process defined on a sphere

is essentially different from that of a stationary process on the Euclidean space. In particular, if $Z(\theta, \phi)$ denotes an axially symmetric process on $\mathbb{S}^2$, then

$$\operatorname{cov}(Z(\theta_1, \phi_1), Z(\theta_2, \phi_2)) = K(\theta_1, \theta_2, \phi_1 - \phi_2),$$

whereas for a stationary process $Z'(x, y)$ on $\mathbb{R}^2$,

$$\operatorname{cov}(Z'(x_1, y_1), Z'(x_2, y_2)) = K(x_1 - x_2, y_1 - y_2).$$

Thus, we cannot apply these tests to check whether the covariance function of a process on the sphere is isotropic. This necessitates the development of a test with a flexible alternative that does not depend on a rigid definition of "stationarity".

Our approach for testing for isotropy on a sphere is similar in spirit to that of Bandyopadhyay and Rao (2017), who propose a test for stationarity on Euclidean spaces based on the discrete Fourier transform (DFT) vector. Here, the elements of the DFT vector are approximately uncorrelated under stationarity on Euclidean spaces. Because isotropic models on spheres are uniquely characterized in terms of the spherical harmonic (SH) representation rather than a Fourier transform, it is natural to formulate a global test for isotropy based on the SH coefficients. In our approach, we transform the data onto the SH functions, which form a set of orthogonal basis functions on the sphere. We exploit the fact that the correlation between the coefficients is zero if the process is isotropic. Furthermore, they are Gaussian if the random field we start with is Gaussian (Baldi and Marinucci (2007)). On the contrary, if the random field is not isotropic, this characterization will not hold. Thus, we formulate our test based on the sample correlation structure between the SH coefficients. This also ensures that the alternative considered in our test is very general, because every anisotropic model has coefficients that are correlated in some manner. We construct our test based on the largest eigenvalue of the sample correlation matrix, which increases as we move away from isotropy, giving us a right-sided critical region for our test. Our approach requires replication across time, and we propose a method to deal with the temporal correlation in the data. The approach is computationally efficient for gridded data because fast Fourier transforms (FFT) aid in the projection of the data onto SHs. The test can also be based on a manageable number of SH coefficients, which means no large dense matrices need to be stored. We also show that the approximations employed in the test improve as the resolution of the data in space increases.

We apply the test to near-surface air temperature projections for 2031–2035 obtained from the Hadley Centre Coupled Climate Model Version 3 (HadCM3). We do not expect these data to be well modeled by an isotropic model. However,

because we can build anisotropic models from isotropic models, we can apply the test to the isotropic component of anisotropic models to check the anisotropic model assumptions. Thus, we propose a sequence of anisotropic models for our temperature data, each more complex than the previous one, and each having an isotropic process as a model component. We apply the proposed test to the isotropic components of the models and consider the values of the test statistic to determine how well the models capture the anisotropy in the near-surface temperature fields.

The rest of the paper is structured as follows. In Section 2, we discuss the HadCM3 data set used in this study. Section 3 illustrates our model and the test procedure. Section 4 presents a simulation study that evaluates the performance of our test under various conditions. Section 5 presents our analysis of the near-surface air temperature data, where we include a thorough discussion of the nature of the anisotropies in the data. Section 6 concludes the paper.

2. Motivating Data Set

The data set that motivated this study is part of the Coupled Model Intercomparison Project Phase 5 (CMIP 5) archive. The CMIP 5 is a large multimodel ensemble project that has been used for the Intergovernmental Panel on Climate Change (IPCC) reports. The HadCM3 of the Met Office Hadley Centre (MOHC) is a coupled climate model that has been used in various climate studies, including climate prediction and climate modeling. The HadCM3 was one of the significant models utilized as part of the IPCC Third and Fourth Assessments, as well as contributing to the Fifth Assessment. These models have a resolution of 2.5 degrees in latitude by 3.75 degrees in longitude, producing a global grid of 73×96 grid cells. This is equivalent to a surface resolution of about 417 km $\times 278$ km at the Equator, reducing to 295 km $\times 278$ km at 45 degrees of latitude. These model simulations also consider a 360-day calendar, where each month has 30 days.

From the HadCM3 outputs in the CMIP 5, we consider the Representative Concentration Pathway 4.5 ("RCP4.5") simulations of daily near-surface air temperature ("tas") in the Kelvin scale for the period of 2031–2035. Our analysis forms part of a larger analysis, where we aim to estimate anisotropic correlations in atmospheric processes across the globe. The sample data illustrate the near-future projections of climate conditions based on a standard set of model simulations, and are known to mimic real-life scenarios fairly consistently

(Schramm et al. (2014)). As mentioned before, the temperature values are generated on a 73 × 96 latitude × longitude grid for 360 days per year, giving a total of approximately 12.6 million observations in the data set.

3. Methodology

3.1. SH representation

Let $Y_t(\theta,\phi), t \in 1,2,\ldots,T$ denote a Gaussian process (GP) on a sphere indexed by latitude $\theta \in [0,\pi]$ and longitude $\phi \in [0,2\pi)$. Because $Y_t(\theta,\phi)$ is a GP, it is completely defined by a mean function $\mu(\theta,\phi) = E\left(Y_t(\theta,\phi)\right)$ and a covariance function $K(\theta_1,\theta_2,\phi_1,\phi_2) = \mathrm{Cov}\left(Y_{t_1}(\theta_1,\phi_1), Y_{t_2}(\theta_2,\phi_2)\right)$. For the time being, the covariance is assumed to be independent over time. However, this assumption is not suitable for spatiotemporal data. We discuss the incorporation of a rich temporal structure in our model using a nonseparable covariance function in Sections 4.2 and 5. Now, an isotropic GP on a sphere can be defined by a constant mean function and a covariance function that depend only on the great circle distance (or equivalently, the chordal distance) between two points on the sphere. That is, if we consider a sphere of radius R, an isotropic process on the sphere has the covariance function

$$K(\theta_1,\theta_2,\phi_1,\phi_2) = f(\mathrm{gcd}(\theta_1,\theta_2,\phi_1,\phi_2)),$$

for some function $f(\cdot)$, and

$$\mathrm{gcd}(\theta_1,\theta_2,\phi_1,\phi_2) = 2R\arcsin\left(\left\{\sin^2\left(\frac{\theta_1-\theta_2}{2}\right)+\cos\theta_1\cos\theta_2\sin^2\left(\frac{\phi_1-\phi_2}{2}\right)\right\}^{1/2}\right).$$

The GP can be expressed in terms of SH basis functions, as suggested by Jones (1963). Let $S_{l,m}(\theta,\phi)$ denote the Schmidt semi-normalized harmonics of degree l and order m on the surface of the sphere. Analytically, $S_{l,m}(\theta,\phi)$ can be defined as

$$S_{l,m}(\theta,\phi) = \begin{cases} \sqrt{\dfrac{(l-m)!}{(l+m)!}}P_{l,m}(\cos\theta)e^{im\phi} & m \geq 0, \\ (-1)^m S^*_{l,-m}(\theta,\phi) & m < 0, \end{cases}$$

where * denotes a complex conjugation and $P_{l,m}(\cos\theta)$ denotes the associated Legendre polynomial of degree $l = 0,1,2,\ldots$ and order $m = 0,1,\ldots,l$; that is,

$$P_{l,m}(x) = (-1)^m(1-x^2)^{m/2}\frac{d^m}{dx^m}P_l(x),$$

$$P_l(x) = \frac{1}{2^l l!}\frac{d^l}{dx^l}(x^2-1)^l.$$

The SHs form a complete set of orthogonal basis functions on the sphere; in particular,

$$\int_{\theta=0}^{\pi}\int_{\phi=0}^{2\pi} S_{l,m}(\theta,\phi)S_{l',m'}(\theta,\phi)^*\sin\theta d\phi d\theta = \frac{4\pi}{(2l+1)}\delta_{ll'}\delta_{mm'},$$

where $\delta_{ij} = \mathbb{1}(i=j)$ is the Kronecker delta. As a result, processes defined on the sphere can be expressed in terms of expansions of the SH functions. Here, we consider

$$Y_t(\theta,\phi) = \sum_{l=0}^{\infty}\sum_{m=-l}^{l} a_{lmt}S_{l,m}(\theta,\phi), \tag{3.1}$$

where $\{a_{lmt}\}$ is a triangular array (for each t), representing the set of complex-valued random SH coefficients for which the sum in (3.1) converges in mean square. Note that because $S_{l,m}(\theta,\phi) = (-1)^m S^*_{l,-m}(\theta,\phi)$, for $m<0$, the coefficients satisfy the identity

$$a_{lm} = (-1)^m a^*_{l,-m}.$$

The random variables $(a_{lmt})_{l,m}$ are uncorrelated and form a Gaussian family if and only if, in addition to being Gaussian, $Y_t(\theta,\phi)$ is also isotropic (Baldi and Marinucci (2007)). Furthermore $E[Re\,(a_{lmt})] = 0 = E\,[Im\,(a_{lmt})]$, for $m = 0,\ldots,l$, and $Re\,(a_{lmt})$ and $Im\,(a_{lmt})$ are uncorrelated with the variance $E\left[Re\,(a_{lmt})^2\right] = E\left[Im\,(a_{lmt})^2\right] = C_l/2$, where C_l is the power spectrum for degree l. Because of the conjugacy between the coefficients for positive and negative m's, the coefficients are only uncorrelated, and not independent, even though they are Gaussian. This is illustrated with the help of an example. Let $z_1 = a+ib$ and $z_2 = a-ib$ denote two complex random variables with $a,b \overset{indpt}{\sim} N(0,\tau^2)$. Now,

$$\mathrm{Cov}(z_1,z_2) = E(z_1z_2^*) = E(a^2-b^2) = \mathrm{Var}(a) - \mathrm{Var}(b) = \tau^2-\tau^2 = 0.$$

However, z_1 and z_2 are not independent because $z_1 = z_2^*$. Thus, for complex conjugate Gaussian random variables, being uncorrelated does not imply independence.

We now have $\mathrm{Var}(a_{lmt}) = E\left[|a_{lmt}|^2\right] = E\left[Re\,(a_{lmt})^2\right] + E\left[Im\,(a_{lmt})^2\right] = C_l$. Because the coefficients are uncorrelated across l and m, the covariance function for $Y_t(\theta,\phi)$ is

$$K(\theta_1,\theta_2,\phi_1,\phi_2) = \sum_{l=0}^{\infty} C_l P_l\left(\sin\theta_1\sin\theta_2\cos(\phi_1-\phi_2) + \cos\theta_1\cos\theta_2\right).$$

Hence, the variance of $Y_t(\theta,\phi)$ is

$$\mathrm{Var}(Y_t(\theta,\phi)) = \sum_{l=0}^{\infty} C_l.$$

The derivation of the formula is provided in Section 1 of the Supplementary Material.

Our testing procedure relies on a transformation from the observations $Y_t(\theta,\phi)$ to the SH coefficients a_{lmt}. If $Y_t(\theta,\phi)$ are observed continuously over the sphere, then the SH transform, given by

$$a_{lmt} = \int_{\theta=0}^{\pi}\int_{\phi=0}^{2\pi} Y_t(\theta,\phi)S_{l,m}(\theta,\phi)\sin\theta d\phi d\theta,$$

can be used to recover the coefficients a_{lmt}. However, if we have data on a grid of size $s_1 \times s_2$, we cannot recover the coefficients exactly. Thus, we estimate a_{lmt} as the minimizer of

$$\sum_{i=1}^{s_1 s_2}\left\{Y_t(\theta_i,\phi_i) - \sum_{l=0}^{l_{reg}}\sum_{m=-l}^{l} a_{lmt}S_{l,m}(\theta_i,\phi_i)\right\}^2 \triangle\, W_i, \tag{3.2}$$

where $\triangle W_i$ is the surface area of the ith quadrangle, relative to the surface area of the Earth, and l_{reg} is chosen such that $(l_{reg}+1)^2 \le s_1 s_2$. For very large gridded data sets, the sums over longitudes and over m can be computed efficiently using FFTs. This is a weighted least squares problem, where the weights are equal to the relative surface area of the quadrangles.

Let $\boldsymbol{Y}_t$ denote the data vector for time t at all spatial locations and $\boldsymbol{Y}$ be the $s_1 s_2 \times T$ matrix $[\boldsymbol{Y}_1,\ldots,\boldsymbol{Y}_T]$. In addition, let $\boldsymbol{S} = (S_{l,m})_{l,m}$ denote the matrix of the semi-normalized harmonics, truncated at degree l_{reg}, and $\boldsymbol{W}$ denote a diagonal matrix, with the weights $\triangle W_i$ on the diagonal. Then, minimizing the sum with respect to a_{lmt} gives the coefficient matrix as $\widehat{\boldsymbol{a}} = (\boldsymbol{S}'\boldsymbol{W}\boldsymbol{S})^{-1}\boldsymbol{S}'\boldsymbol{W}\boldsymbol{Y}$. We apply this transformation at each time point, and use $\widehat{\boldsymbol{a}}_{lm\bullet} = (\widehat{a}_{lm1},\ldots,\widehat{a}_{lmT})$ to denote the SH coefficient corresponding to degree l and order m, replicated over time. We use $\widehat{\boldsymbol{a}}_{\bullet t}$ to denote all coefficients at time point t.

3.2. Test procedure

Because we truncate the sum in (3.1) to represent the process, we work with a total of $n_{reg} = (l_{reg}+1)^2$ SHs. We explore the selection of the truncation degree l_{reg} in Section 4, based on the stability of the regression that converts $\boldsymbol{Y}$ to $\widehat{\boldsymbol{a}}$. Depending on the accuracy of the regression, we only use SHs up to degree $l_{corr} \le l_{reg}$ and use $p = n_{corr} = (l_{corr}+1)^2$ coefficients in the test. The selection of l_{corr} is also described in Section 4. Because the true coefficients $\boldsymbol{a}$

are uncorrelated under isotropy, our hypotheses about isotropy are equivalent to

$$H_0 : R = I_p \qquad \text{versus} \qquad H_1 : R \neq I_p,$$

where $R = \text{Corr}(\boldsymbol{a}_{\bullet t})$.

We construct the test statistic based on the eigenvalues of the sample correlation matrix of $\widehat{\boldsymbol{a}}_{\bullet 1}, \ldots, \widehat{\boldsymbol{a}}_{\bullet T}$. Under the null hypothesis, the eigenvalues of the population correlation matrix will all be one, and when we move away from the null, the largest sample eigenvalue will increase. This motivates us to create a test based on the largest sample eigenvalue. Johnstone (2001) provides the distribution of the largest eigenvalue of the sample covariance matrix when sampling from a multivariate normal distribution with a covariance matrix equal to the identity matrix. Johnstone (2001) also provides an ad hoc construction method to make the distribution in order to test the above-mentioned hypothesis. For this purpose, let $\boldsymbol{w}_{lm\bullet}$ denote the standardized SH coefficient corresponding to degree l and order m. Notationally,

$$\boldsymbol{w}_{lm\bullet} = \frac{\widehat{\boldsymbol{a}}_{lm\bullet}}{\|\widehat{\boldsymbol{a}}_{lm\bullet}\|}.$$

The vectors $\boldsymbol{w}_{lm\bullet}$ have a sample variance equal to one. Now, we multiply each standardized SH coefficient by an independent chi random variable in order to generate a standard Gaussian data matrix, denoted by $\tilde{\boldsymbol{a}}^{(p)} = (\tilde{\boldsymbol{a}}_{lm\bullet})_{l,m}$, where

$$\tilde{\boldsymbol{a}}_{lm\bullet} = r_{lm}\boldsymbol{w}_{lm\bullet}, \qquad r_{lm}^2 \overset{indep}{\sim} \chi_T^2.$$

Multiplying r_{lm} by w_{lmt} is critical to the proposed method because the theorem stating the distribution of the largest eigenvalue does not directly apply to sample correlation matrices. Now, the test statistic is

$$\tilde{l}_1 = \frac{l_1(\tilde{\boldsymbol{C}}) - \mu_{Tp}}{\sigma_{Tp}},$$

where $l_1(\tilde{\boldsymbol{C}})$ is the largest sample eigenvalue of $\tilde{\boldsymbol{C}} = \tilde{\boldsymbol{a}}^{(p)\prime}\tilde{\boldsymbol{a}}^{(p)}$, $\mu_{Tp} = (\sqrt{T-1} + \sqrt{p})^2$, and $\sigma_{Tp} = (\sqrt{T-1}+\sqrt{p})(1/\sqrt{T-1}+1/\sqrt{p})^{1/3}$. Under the null hypothesis, when T and p both increase, such that $T/p \to \gamma \geq 1$,

$$\tilde{l}_1 \xrightarrow{d} W_1 \sim F_1,$$

where F_1 is the Tracy–Widom law of order 1 (described in Section 2 of the Supplementary Material).

The test is designed for $T \geq p$, but it applies equally well if $T < p$ are both large. In this case, we simply reverse the roles of T and p in the expressions for μ_{np} and σ_{np} (Johnstone (2001)). The p-value for the test is computed using the

cumulative distribution table of the TW_1 distribution (Bejan (2005)). Because the largest eigenvalue increases as the spatial process becomes more anisotropic, we have a right-tailed test.

4. Simulation Study

4.1. Stability of the SH estimates

In this section, we first verify that the weighted regression technique in (3.2) gives accurate coefficient estimates $\widehat{\boldsymbol{a}}$ when we truncate the sum in (3.1). For this purpose, we choose $l_{sim} > l_{reg}$ and simulate $n_{sim} = (l_{sim}+1)^2$ Gaussian complex-valued coefficients $\boldsymbol{a}(n_{sim} \times T)$ with variance C_l, independent over $T = 360$ time replicates, and then apply (3.1) to obtain the spatial data, $Y_t(\theta, \phi)$ (forward transform). We evaluate how well we recover $\boldsymbol{a}$ when we regress the data $\boldsymbol{Y}$ onto $\boldsymbol{S}$, the SHs truncated at l_{reg} (back transform).

For the variance of $Y_t(\theta, \phi)$ to exist, C_l must be summable. To achieve this, we consider the variances

$$C_l = \frac{\sigma^2}{(\alpha^2 + l^2)^{\nu+1/2}},$$

which gives rise to the Legendre–Matérn covariance function (Guinness and Fuentes (2016)) given by

$$\psi(\theta) = \sum_{l=0}^{\infty} \frac{\sigma^2}{(\alpha^2 + l^2)^{\nu+1/2}} P_l(\cos\theta).$$

Here, $\sigma^2, \alpha, \nu > 0$ are the three parameters of the covariance function, with σ^2 denoting the variance, $1/\alpha$ denoting the spatial range, and ν the smoothness. The form of the Legendre Matérn is motivated by the Matérn spectral density on $\mathbb{R}^d$, which is $(\alpha^2 + \omega^2)^{-\nu-1/d}$. In particular, we set $\nu = 0.5$ and $\nu = 1$ for our simulation studies. This gives us C_l of the order of $1/l^2$ and $1/l^3$, respectively. For convenience, we refer to the two spectra as C_{l2} and C_{l3}, respectively. Note that the process obtained from $C_{l2}(\nu = 0.5)$ is not mean-square differentiable. According to Hitczenko and Stein (2012), this is similar to a process with an exponential covariance.

In order to ensure computational stability during the regression (back transform), we choose the truncation degree of the SH, l_{reg}, based on the condition number of $\boldsymbol{S}'\boldsymbol{W}\boldsymbol{S}$, that is, the ratio of its smallest eigenvalue to its largest. We choose the largest l such that the condition number of $\boldsymbol{S}'\boldsymbol{W}\boldsymbol{S} > 0.001$. The regenerated coefficients are

$$\widehat{\boldsymbol{a}}_{\bullet t} = (\boldsymbol{S}'\boldsymbol{W}\boldsymbol{S})^{-1}\boldsymbol{S}'\boldsymbol{W}\boldsymbol{Y}_t.$$

Here, $\widehat{\boldsymbol{a}}_{\bullet t}$ is of length n_{reg}, because $\boldsymbol{S}$ is of order $n_{reg} \times s_1 s_2$, whereas $\boldsymbol{a}_{\bullet t}$ is of length n_{sim}, which is much larger than n_{reg} because $l_{sim} > l_{reg}$.

The accuracy of the regression is summarized by the correlation between the unique real and imaginary parts of the true coefficients for each l and the corresponding estimates,

$$r_l = \frac{1}{2l+1} \sum_{m=-l}^{l} Corr(\boldsymbol{a}_{lm\bullet}, \widehat{\boldsymbol{a}}_{lm\bullet}),$$

where

$$Corr(\boldsymbol{a}_{lm\bullet}, \widehat{\boldsymbol{a}}_{lm\bullet}) = \frac{\sum_{t=1}^{T}(a_{lmt} - \bar{a}_{lm})(\widehat{a}_{lmt} - \widehat{a}^b_{lm})}{\sqrt{\sum_{i=1}^{T}(a_{lmt} - \bar{a}_{lm})^2}\sqrt{\sum_{i=1}^{T}(\widehat{a}_{lmt} - \widehat{a}^b_{lm})^2}},$$

and $\bar{a}_{lm} = (1/T)\sum_{t=1}^{T} a_{lmt}$ and $\widehat{a}^b_{lm} = (1/T)\sum_{t=1}^{T} \widehat{a}_{lmt}$ denote the means of $\boldsymbol{a}_{lm\bullet}$ and $\widehat{\boldsymbol{a}}_{lm\bullet}$, respectively. Figure 1 shows that the correlation between the true and estimated SH coefficients is a decreasing function of l_{reg}. This motivates us to choose l_{corr} as the maximum degree of SH for which $r_l > 0.999$. This ensures that the weighted regression in (3.2) gives accurate SH coefficients, as long as the degree of SH considered is less than or equal to l_{corr}. We also wish to study the effect of the grid size on the performance of the weighted regression. With this in mind, we use three different grid sizes, namely $20 \times 50, 73 \times 96$, and 100×200 for our study. In all of our numerical studies, l_{sim} is chosen to be 150. Figure 1 also shows that the regression performs better as the grid size increases and as the spectra decrease. Table 1 illustrates how both the number of SHs used for a meaningful regression and the accuracy of the coefficient estimations grow with l^2. Table 1 actually shows the maximum number of SHs one can use in order to get stable and accurate estimates of the coefficients. However, we are performing the test on a relatively small number of SH coefficients relative to the grid size, which can be determined from the power curve (illustrated in a subsequent section). In our data analysis, we have a grid of size 73×96. Our numerical study indicates that under spectrum C_{l2}, we can use l_{corr} up to 30, which corresponds to constructing a test on at most $(30+1)^2 = 961$ unique coefficients.

In the next subsection, we assess the performance of our test. First, we calculate the Type-I error of the test by generating time-independent coefficients under the null. Next, we consider the temporal correlation between the coefficients. Finally, we compute the power of the test under anisotropic models.

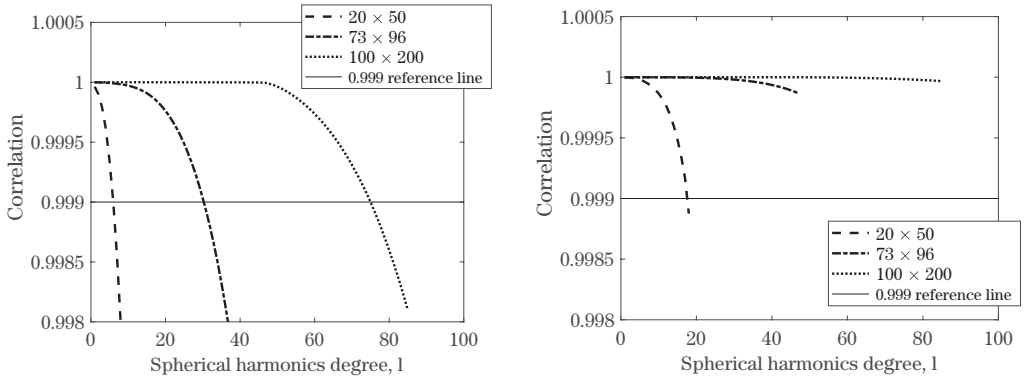

(a) Spectrum C_{l2} (b) Spectrum C_{l3}

Figure 1. Correlation between the true and estimated coefficients for the three different grid sizes, 20×50, 73×96, and 100×200 and for two different spectra (left versus right) as a function of the SH degree l. We consider the SH degree up to l_{reg} in the weighted regression. For each grid size–spectra combination, we take l_{corr} as that value of l where the corresponding correlation curve intersects the 0.999 reference line, which gives us $n_{corr} = (l_{corr} + 1)^2$ unique coefficients.

Table 1. The maximum degree of SH that ensures computational stability during a regression, l_{reg}, and the maximum degree of SH used to guarantee an accurate estimation of the coefficients, l_{corr}, for the three different grid sizes and the two spectra. n_{reg} and n_{corr} give the number of SH functions used in each setting. l_{sim} is chosen to be 150.

Spectrum	Grid Size	l_{reg}	n_{reg}	l_{corr}	n_{corr}
C_{l2}	20×50	18	361	6	49
	73×96	47	2,304	30	961
	100×200	85	7,396	74	5,625
C_{l3}	20×50	18	361	17	324
	73×96	47	2,304	47	2,304
	100×200	85	7,396	85	7,396

4.2. Assessing the performance of the test

Type-I error under no temporal correlation

We simulate a_{00} from $N(0, 1.5)$ and the other coefficients as time-independent complex Gaussian, that is,

$$Re\ a_{lmt}, Im\ a_{lmt} \sim N\left(0, \frac{C_l}{2}\right), l = 1, \ldots, l_{sim}, t = 1, \ldots, T = 360,$$

with $l_{sim} = 150$ and for C_{l2} and C_{l3}. We follow the test procedure described in Section 3 for the three grid sizes 20×50, 73×96, and 100×200 with appropriate choices of l_{reg} and l_{corr}, as described in Table 1. We perform the test at the 5%

Table 2. Type-I error (in %) of the test for the three grid sizes, 20×50, 73×96, and 100×200, and the two spectra, C_{l2} and C_{l3}. We perform the test at the 5% significance level. Here, l represents the SH degrees for which we perform the test. Note that for a particular setting, we only consider l less than or equal to the corresponding l_{corr}. The estimated two standard error limits (in percentages) for the empirical Type-I error rates are (3.6, 6.4). All empirical Type-I error rates fall within these limits, which shows that they are very close to the nominal error rate of 5%.

20×50			73×96			100×200		
l	C_{l2}	C_{l3}	l	C_{l2}	C_{l3}	l	C_{l2}	C_{l3}
3	4.3	3.4	5	4.7	5.6	5	5.3	5.3
4	5.2	3.6	10	4.8	3.7	10	5.4	5.4
5	5.0	5.3	15	5.2	3.6	15	4.9	4.9
8		4.3	20	4.7	3.7	25	3.6	3.6
10		5.2	24	4.9	5.4	35	5.0	4.8
15		5.8	27	4.8	5.6	45	4.9	4.9
			29	4.7	3.7	55	5.8	5.5
			35		4.5	65	4.9	4.7
			40		4.3	70	4.7	4.8
			45		4.4	74	5.6	5.5
			47		5.2	80		4.2
						85		5.0

significance level. The Type I error of the test is given by

$$p = Pr_{H_0}(TW(T,p) > T_{obs}) = Pr_{H_0}\left(TW_1 > \frac{T_{obs} - \mu_{Tp}}{\sigma_{Tp}}\right).$$

Table 2 shows the Type-I error of the test for the three grid sizes and two different spectra based on 1,000 simulation replications. The Type-I error varies between 3% and 6%, depending on the choice of l. The estimated two standard error limits (in percentages) for the empirical Type-I error rates are (3.6, 6.4). All empirical Type-I error rates fall within these limits, which shows that they are very close to the nominal error rate of 5%.

Type-I error under temporal correlation

Our test requires replications of the spatial process and, for most applications, the replications will be correlated in time. Based on our analysis of the climate temperature data in Section 5 and on previous studies of space–time covariances (Stein (2005)), we expect the lower degree coefficients to have a stronger temporal correlation than those of the higher degree coefficients. For our simulation study, we assume a simple AR(1) structure between the coefficients. For $t = 1, \ldots, T = 360$,

$$a_{lmt} = \rho_{lm} a_{lm(t-1)} + e_{lmt},$$

Table 3. Type-I error (in %) of the test for the three grid sizes, 20×50, 73×96, and 100×200, and the two different spectra, C_{l2} and C_{l3}, after accounting for temporal correlation. We perform the test at the 5% significance level.

20×50			73×96			100×200		
l	C_{l2}	C_{l3}	l	C_{l2}	C_{l3}	l	C_{l2}	C_{l3}
3	4.7	3.7	5	4.7	4.3	5	4.7	5.3
4	4.3	4.1	10	4.6	4.5	10	4.4	5.1
5	4.4	6.0	15	4.8	4.4	15	4.8	5.1
8		5.0	20	4.9	4.8	25	4.6	5.1
10		5.2	24	5.0	5.1	35	5.2	4.9
15		5.9	27	5.3	5.0	45	4.9	5.4
			29	4.5	5.4	55	4.4	5.0
			35		5.7	65	4.2	4.5
			40		4.3	70	4.1	4.8
			45		5.7	74	4.9	5.0
			47		5.3	80		4.3
						85		4.3

where the innovations e_{lmt} are uncorrelated across l, m, and t, and $e_{lmt} \sim CN(0, C_l)$. In addition, $\rho_{lm} = 0.9/\sqrt{l}$, for $l = 1, 2, \ldots, l_{sim}$, with $\rho_0 = 0.99$, is the temporal correlation function that decays with the degree of the SH. The simulated data are transformed to real space using the forward-transform (3.1).

To illustrate the importance of addressing the temporal dependence in spatiotemporal data, we perform the test directly on the coefficients obtained from back-transforming the data into SH coefficients. In such a scenario, the Type-I error of the test is more than 99% for each of the grid sizes and spectra, even when the underlying spatial covariance structure is isotropic.

To account for temporal dependence in our test, we treat $\widehat{\boldsymbol{a}}_{lm\bullet}$, obtained from the back transform as a time series, and estimate ρ_l for every (l, m) combination by regressing $\widehat{a}_{lm2}, \ldots, \widehat{a}_{lmT}$ on $\widehat{a}_{lm1}, \ldots, \widehat{a}_{lm(T-1)}$. We then perform the test on the innovations at the 5% significance level. Table 3 shows the Type-I error of our test after accounting for temporal dependence. Once again, we see that the test has the right size.

Power computations

In this section, we study the power of our test for anisotropic data. We consider a few important departures from an isotropic process. In the first scenario, we consider a process that is axially symmetric. According to Jones (1963), an axially symmetric process is one in which the covariance at a pair of locations is a function of the two latitudes and the difference in their longitudes. That

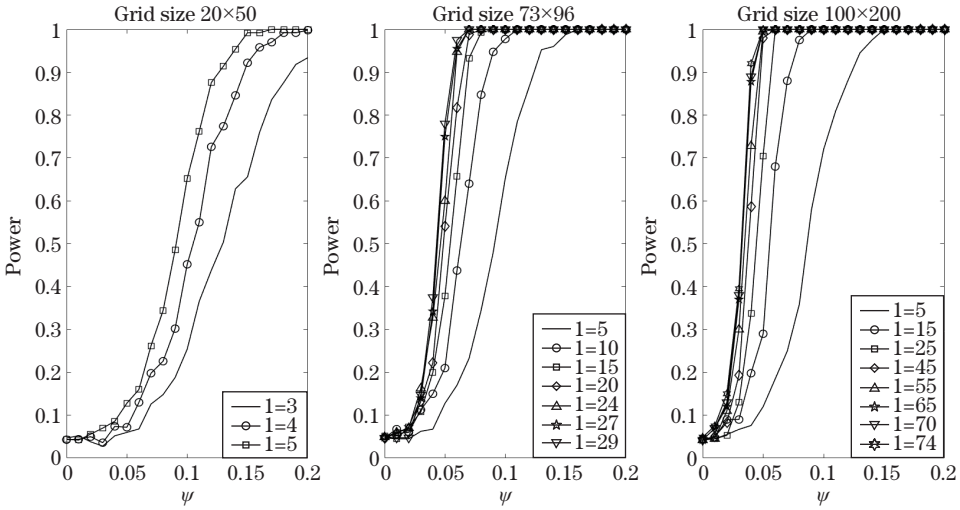

Figure 2. Empirical power functions of our test (as a function of ψ) corresponding to Scenario 2 (axially symmetric process) for the three grid sizes and different degrees of SH, l.

is, $K(\theta_1, \theta_2, \phi_1, \phi_2) = g(\theta_1, \theta_2, \phi_1 - \phi_2)$ for some function $g(\cdot)$. Jones (1963) also gives us a necessary and sufficient condition for a process to be axially symmetric in terms of the SH coefficients, given by

$$\mathrm{Cov}(a_{lmt}, a_{l'm't}) = 0,$$

for $m \neq m'$. Under this scenario, we generate a_{lmt} as complex Gaussian with variance C_{l2}, defined by

$$a_{lmt} = \sqrt{C_{l2}}(B_{lmt} + e_{lmt}),$$

where B_{lmt} is complex Gaussian with variance 0.5 and

$$\mathrm{Corr}(B_{lmt}, B_{l'm't}) = \begin{cases} 0 \;\; l \neq l', m \neq m', \\ \psi \; l \neq l', m = m', 0 \leq \psi \leq 1. \end{cases}$$

Here, e_{lmt} is complex Gaussian with variance 0.5 and independent across l and m. Figure 2 plots the power by ψ for the three grid sizes 20×50, 73×96, and 100×200. All results are based on 1,000 simulation replications and $T = 360$ independent time replications for each simulation replication. For each of the 1,000 data sets, we conduct the test with suitable l_{reg}, as mentioned in Table 1, and a few suitable l's, as listed in Table 2.

Figure 2 shows that the test is powerful in detecting small departures from isotropy for reasonable grid sizes and with a relatively small degree of the SHs.

We see that the power increases with the degree of the SH functions used in our analysis. The power also increases as the data points on the sphere become more dense.

Another way to introduce anisotropy directly into the fields is to assume that the covariance structures over different parts of the globe are different. A simple way to do this is to consider different covariances over land and water. In particular, we define

$$g_l(s) = \begin{cases} 1, & \text{if } s \in land, \\ 1/l^{\epsilon}, & \text{if } s \in ocean, \end{cases}$$

where $\epsilon \geq 0$; $\epsilon = 0$ is the case of isotropy. The fields are then generated as

$$Y_{\text{aniso};t}(s) = \sum_{l=0}^{l_{sim}} \sum_{m=-l}^{l} g_l(s) a_{lmt} S_{l,m}(\theta, \phi),$$

where a_{lmt}, for $t = 1, \ldots, T = 360$, is simulated as complex Gaussian with variance C_{l2} and independent over time. Because $\epsilon > 0$, $g_l(s)$ has the effect of reducing the variance of the high-frequency coefficients, resulting in smoothing processes over the ocean. Figure 3 plots the empirical power functions of our test as a function of ϵ. The other settings are the same as those in Figure 2. Once again, we consider 1,000 simulation replications to estimate the power function. The results confirm that the test is powerful, even for very minor departures from isotropy, with $\epsilon < 0.1$. We also see that the power of the test increases with the degree of the SH used in our analysis and with the grid size.

The power computations for another anisotropic model are provided in Section 3 of the Supplementary Material. The power curves can be used to determine the number of SH coefficients that we actually need to consider to construct the test. If we consider the power curves for the different scenarios corresponding to the grid size 100×200, we do not gain much in terms of power if we increase l beyond 25. This makes our method feasible when we are working with huge data sets, because we do not need to work with high-dimensional matrices. For the real-data application, we have chosen the SH degree to be 25, which means we are working with $(25 + 1)^2 = 26^2 = 676$ SH functions.

5. Application to HadCM3 Output Data

We apply our method to near-surface air temperature data obtained as output from the HadCM3. We work with daily air temperature data for the period 2031–2035, projected onto a 73×96 grid in latitude and longitude. Each month

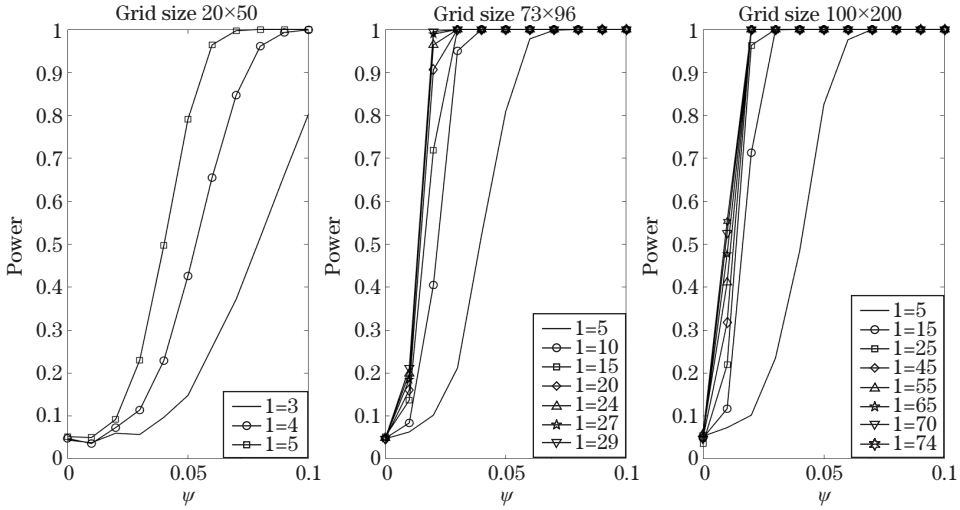

Figure 3. Empirical power functions of our test (as a function of ϵ) corresponding to Scenario 2 for the three grid sizes and different degrees of SH, l.

in the data has 30 days. Thus, we have data for five years with 360 time points corresponding to each year, resulting in $T = 1{,}800$ time points. Although we do not believe that the temperature fields are isotropic, we use the test to estimate the goodness of fit of the models that seek to remove the anisotropies in the fields. We consider a few anisotropic models based on isotropic processes, and perform the test on the isotropic component of each model. In each of the models, $Y_t(\theta, \phi)$, for $t = 1, \ldots, T$, denotes the near-surface air temperature at location $(\theta, \phi), \theta \in [0, \pi], \phi \in [0, 2\pi)$. We consider three models of increasing complexity. Each model M_i can be written in the form

$$Y_t(\theta, \phi) = m_t^{(i)}(\theta, \phi) + e_t^{(i)}(\theta, \phi),$$
$$\frac{1}{k^{(i)}(\theta, \phi)} e_t^{(i)}(\theta, \phi) = \sum_l \sum_m a_{lmt} S_{l,m}(\theta, \phi),$$
$$a_{lmt} = \rho_{lm} a_{lm(t-1)} + \epsilon_{lmt},$$

where $\epsilon_{lmt} \sim N\left(0, \sigma_{lm}^2\right)$. Table 4 describes the form of $m_t^{(i)}(\theta, \phi)$ and $k^{(i)}(\theta, \phi)$ for each of the models considered.

The first model, M_1, has only a spatially varying mean, and M_2 has a pixel-wise seasonal variation in its mean structure along with the spatially varying mean. Then, M_3 additionally takes into account the spatially varying variance. In Section 4.2, we discussed how temporal correlation in the data, if not ac-

Table 4. Description of the three models considered. Here, $b_0, b_1, b_2 \in \mathbb{R}$ and $\sigma^2(\theta,\phi)$ denotes the spatially varying variance.

Model Name	Model Description
M_1	$m_t^{(1)}(\theta,\phi) = b_0(\theta,\phi)$ $k^{(1)}(\theta,\phi) = 1$
M_2	$m_t^{(2)}(\theta,\phi) = b_0(\theta,\phi) + b_1(\theta,\phi)\sin\left(2\pi\frac{t}{360}\right) + b_2(\theta,\phi)\cos\left(2\pi\frac{t}{360}\right)$ $k^{(2)}(\theta,\phi) = 1$
M_3	$m_t^{(3)}(\theta,\phi) = b_0(\theta,\phi) + b_1(\theta,\phi)\sin\left(2\pi\frac{t}{360}\right) + b_2(\theta,\phi)\cos\left(2\pi\frac{t}{360}\right)$ $k^{(3)}(\theta,\phi) = \sigma(\theta,\phi)$

counted for, can produce misleading results when checking whether a process is isotropic. Thus, in each of our models, we model the temporal dependencies in the SH coefficients as AR(1), assuming that the AR coefficients and the innovation variance vary with each (l,m) combination. For each of the models, the spatially varying mean, b_0, is estimated by the pixel-wise mean temperature,

$$\widehat{b}_0(\theta,\phi) = \frac{1}{1{,}800}\sum_{t=1}^{1{,}800} Y_t(\theta,\phi),$$

as illustrated in Figure 4. Here, $b_1(\theta,\phi)$ and $b_2(\theta,\phi)$ are estimated by minimizing the following squared error criteria at each (θ,ϕ):

$$\mathrm{SSE}(\theta,\phi) = \sum_{t=1}^{1{,}800}\left\{Y_t(\theta,\phi) - \widehat{b}_0(\theta,\phi) - b_1(\theta,\phi)\sin\left(2\pi\frac{t}{360}\right) + b_2(\theta,\phi)\cos\left(2\pi\frac{t}{360}\right)\right\}^2.$$

The other parameters in M_2 and M_3, namely ρ_{lm} and σ^2_{lm} are estimated at each pixel (θ,ϕ) by regressing the last $T-1$ SH coefficients on the first $T-1$ coefficients. We use an SH degree of $l = 25$, and work with $(l+1)^2 = 26^2 = 676$ SH coefficients, which means the sample correlation matrix of the coefficients is 676×676 for each of the three models. When applied to the isotropic components of the models, the test yields test statistic values of 958.83, 716.53, and 328.63 for M_1, M_2, and M_3, respectively. This shows that, as the model complexity increases, the models do a better job of explaining the anisotropy in the temperature fields. However, even for the most complex model considered, we obtain a strong rejection of the isotropic component because the value of the test statistic for model M_3 is much larger than that of a TW_1 distribution with a 99th percentile point of 2.02. The

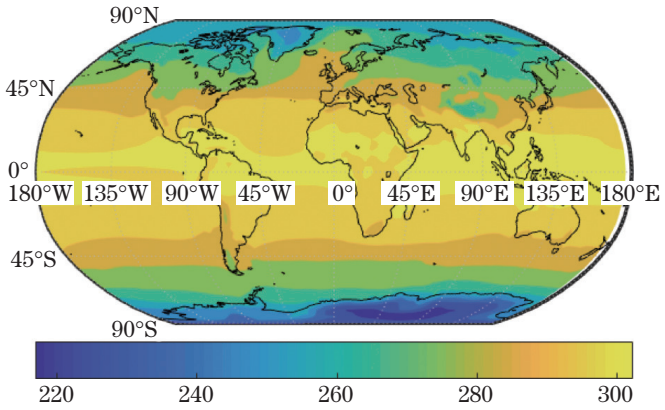

Figure 4. Pixel-wise mean air temperature (in Kelvin) based on five years of model-output data.

AR(1) coefficient estimates and the estimated innovation variance corresponding to the different degrees of SH for M_3 are shown in Figure 5(a).

Figure 5(b) enables us to visualize the SH functions more clearly. When the SH order m is zero, the SH functions do not vary with longitude. In addition, with an increase in $|m|$, the SH functions start to have more SHs along the longitudinal axis and converge to zero at the poles at a faster rate, creating a checkerboard pattern on the sphere until $l = |m|$ has all of the harmonics along the longitude. Figure 5(a) shows that, for each degree, the $m = 0$ coefficient is the most correlated in time and the dependence decreases with an increase in $|m|$. This spectral representation is analogous to the two-dimensional Fourier transform, where each combination of the pair (m, n) corresponds to a two-dimensional frequency. Thus, based on Figure 5(a), we can say that the low-frequency coefficients are very highly correlated in comparison with the high-frequency coefficients. Because the SHs are aligned along the latitudinal direction for $m = 0$ and start to become aligned along the longitudes as $|m|$ increases, we can say that the temperature process is more correlated along the direction of the latitudes than it is along the longitudes. Figure 5(a) also shows the power spectrum of the spectral representation for Model M_3. It shows the strength of each frequency signal and tells us that lower frequencies are, in general, more important than higher frequencies. In particular, the SHs between degrees 7 and 12 seem to be the most meaningful in terms of explaining the process. The spectral densities for models M_1 and M_2 have dominant peaks at low frequencies, overshadowing all other peaks. This is due to the low-frequency variation not

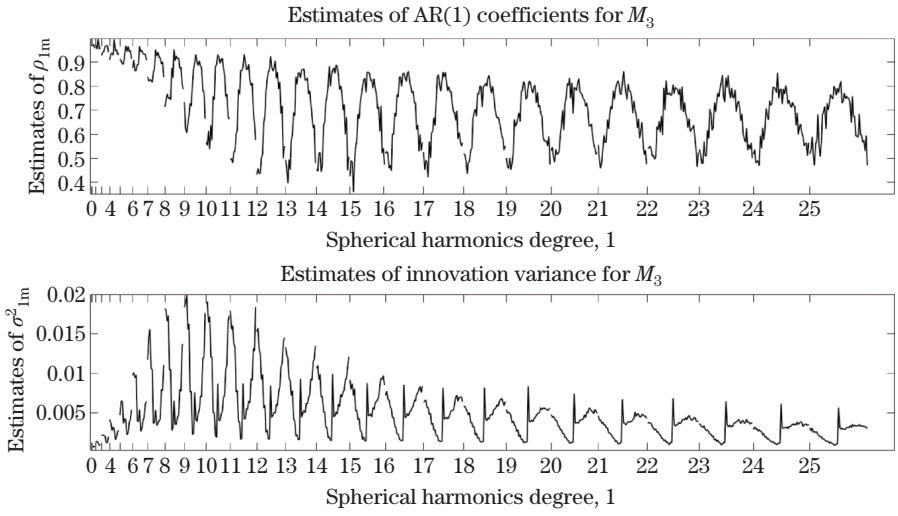

(a) Parameter estimates for M_3

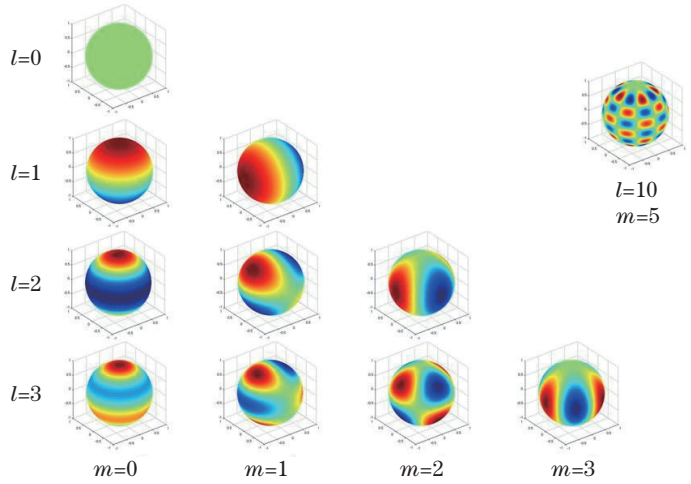

(b) SH functions

Figure 5. (a) Estimates of ρ_{lm} and σ^2_{lm} corresponding to $m = -l, \ldots, -1, 0, 1, \ldots, l$, under each l for M_3. (b) SH functions for $m = 0, \ldots, l$, for $l = 0, \ldots, 3$. The SHs for negative m can be depicted by rotating the positive order ones along the z-axis by $90^\circ/m$. The checkerboard pattern is shown for $l = 10, m = 5$.

being captured by the spatially varying variance.

The innovations from M_3 are still not isotropic, and we point out a few locations attributable to the anisotropy in the process. We estimate the anisotropic covariance of the innovation process from the covariance of the innovation coeffi-

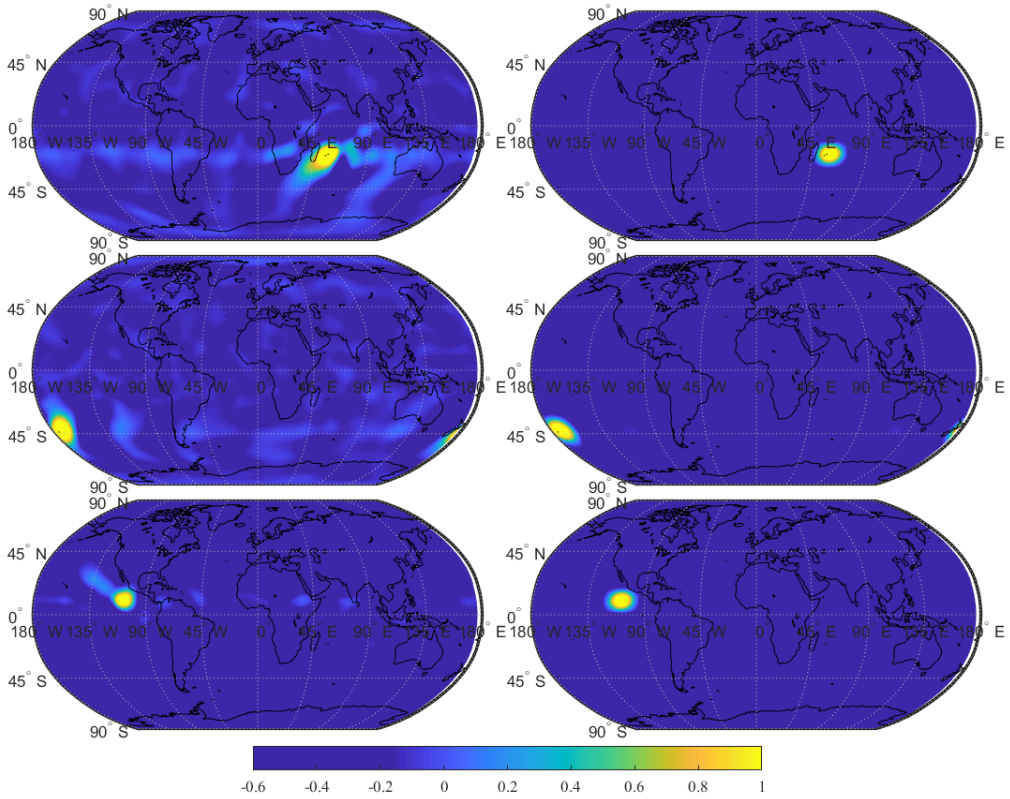

Figure 6. Estimates of the anisotropic (left panel) and (hypothetical) isotropic (right panel) correlation functions at three locations around the globe, namely, northeast of Mauritius (first row), around the 45° S latitude and the International Date Line (second row), and North Pacific Ocean, off the coast of Mexico (third row).

cients. If $\boldsymbol{a}_{innov}$ denotes the innovation coefficients, then the estimate of the covariance illustrating the remaining anisotropy is given by $Cov_{ani} = \boldsymbol{S}Cov(\boldsymbol{a}_{innov})\boldsymbol{S}'$. In contrast, if the process were isotropic at this stage, the covariance matrix of the innovation coefficients would be diagonal. Thus, to estimate the hypothetical isotropic covariance, we shrink all of the off-diagonal elements of $Cov(\boldsymbol{a}_{innov})$ to zero. The locations with a large deviation between the absolute values of the estimated covariances are the main sites contributing to the anisotropy of the near-surface air temperature fields on Earth. Figure 6 shows these locations, along with the anisotropic and isotropic spatial covariances.

The first location chosen is to the northeast of the islands of Réunion and Mauritius, located to the east of Madagascar in the western Indian Ocean. The

covariance structures of this location are shown in Figure 6, row 1. The near-surface air temperature anomalies in this region are associated with outgoing longwave radiation (OLR) anomalies over the west Pacific Ocean (Misra (2004)), as well as with rainfall anomalies over eastern South Africa, which can potentially affect temperatures in the western and southwestern Indian Ocean (Reason and Mulenga (1999)). Row 2 of Figure 6 corresponds to our second location, which is in the south Pacific Ocean, just above the 45° S latitude and slightly to the right of the International Date Line. This is linked to low-frequency variations in the atmospheric circulation over the Southern Hemisphere extratropics (Carleton (2003)). This coincides with the Southern Oscillation, which is characterized by the barometric difference between Darwin and Tahiti. Fluctuations in this difference cause temperature anomalies in parts of the western Pacific, leading to large anisotropies in the temperature covariance. The third location (Figure 6, row 3) is in the north Pacific Ocean, off the coast of Mexico. This location is at the junction of the Pacific/North American teleconnection pattern prevalent over the central north Pacific and the equatorial Pacific Ocean, which is the El Niño zone. This accounts for the temperature anomalies in this area, causing the covariance structure in the temperature fields to move away from isotropy.

6. Discussions and Conclusions

With the availability of large-scale global climate data, it is necessary to develop spatiotemporal models on a sphere that explain the underlying spatial process and help make accurate predictions. It might be convenient to assume that the covariance structure on the globe is isotropic. However in most real-life applications, this assumption does not hold. Therefore, we have proposed a method to determine the aptness of this simplifying assumption.

We assume that a particular meteorological variable is distributed as a GP on a sphere, and we express the process as a linear combination of the SH functions, which form a complete set of orthogonal basis functions on the sphere. Under isotropy, the SH coefficients are uncorrelated and Gaussian (Baldi and Marinucci (2007)). We use this characterization of the coefficients to set up a test for isotropy based on the sample correlation between the coefficients. The test statistic, based on Johnstone (2001), is given in Section 3.2. We provide the conditions necessary to ensure computational stability and accuracy during the regression in Section 4.1.

In Section 4.2, we perform an extensive simulation study to evaluate the

performance of our test. We examine the Type-I errors for three grid sizes and two different spectra under time independence and considering a simple AR(1) dependence in time. The grid sizes are similar to the data resolutions generally observed in real-life applications. Our simulation results show that the test has the right Type-I error for all three grid sizes and under the different conditions. We also consider the power of our test under two anisotropic models. Figures 2 and 3 show that the test is able to detect slight deviations from isotropy in all three scenarios. Furthermore, the power of the test increases as the resolution of the grids become finer. In addition, the power increases with the number of SH coefficients used to compute the sample correlation matrix, which, in turn, depends on the maximum degree of the SH considered.

We show how the test is sensitive to temporal correlation, and provide a modeling framework to address the temporal correlation that gives accurate Type-I error rates. This is demonstrated in Section 4.2, where we consider a decaying temporal correlation between the coefficients and perform the test before and after modeling the temporal dependencies. Most spatiotemporal processes are not isotropic, and our method provides a way to objectively perform a test to help arrive at that conclusion. Furthermore, we can easily determine the possible locations in the data attributed to the anisotropy using our method. As seen in our data analysis, even for the most complex model considered, the test for isotropy is rejected. This highlights the need for better anisotropic models that capture the global anisotropic covariance structures of spatiotemporal processes.

Supplementary Materials

The Supplementary Material provides the derivation of the covariance function, a description of the Tracy Widom law of order 1, and power computations for another anisotropic model.

Acknowledgment

We would like to thank Dr. Dorit Hammerling for bringing the CMIP 5 data archive to our attention and also for her insightful comments during the course of this work. We also acknowledge the World Climate Research Programme's Working Group on Coupled modeling, which is responsible for CMIP, and we thank the MOHC for producing and making available their model output. This material is based upon work supported by the National Science Foundation under Grant No. 1613219. Additionally, Reich and Guinness were partially supported

by the National Institutes of Health Grant R01ES027892.

References

Baczkowski, A. J. and Mardia, K. V. (1990). A test of spatial symmetry with general application. *Communications in Statistics-Theory and Methods* **19**, 555–572.

Baldi, P. and Marinucci, D. (2007). Some characterizations of the spherical harmonics coefficients for isotropic random fields. *Statistics & Probability Letters* **77**, 490–496.

Bandyopadhyay, S. and Rao, S. S. (2017). A test for stationarity for irregularly spaced spatial data. *Journal of the Royal Statistical Society: Series B (Statistical Methodology)* **79**, 95–123.

Bejan, A. (2005). Largest eigenvalues and sample covariance matrices. Tracy-Widom and Painleve II: computational aspects and realization in S-Plus with applications. *Mathematics Subject Classification, 1991*.

Bowman, A. W. and Crujeiras, R. M. (2013). Inference for variograms. *Computational Statistics & Data Analysis* **66**, 19–31.

Cabana, E. M. (1987). Affine processes: a test of isotropy based on level sets. *SIAM Journal on Applied Mathematics* **47**, 886–891.

Carleton, A. M. (2003). Atmospheric teleconnections involving the southern ocean. *Journal of Geophysical Research: Oceans* **108**.

Cressie, N. A. (1993). *Statistics for Spatial Data.* Wiley, New York.

Diggle, P. J. (1981). Binary mosaics and the spatial pattern of heather. *Biometrics*, 531–539.

Fuentes, M. (2007). Approximate likelihood for large irregularly spaced spatial data. *Journal of the American Statistical Association* **102**, 321–331.

Guan, Y., Sherman, M. and Calvin, J. A. (2004). A nonparametric test for spatial isotropy using subsampling. *Journal of the American Statistical Association* **99**, 810–821.

Guinness, J. and Fuentes, M. (2016). Isotropic covariance functions on spheres: Some properties and modeling considerations. *Journal of Multivariate Analysis* **143**, 143–152.

Haskard, K. A. (2007). An anisotropic Matern spatial covariance model: REML estimation and properties. *Doctoral Dissertation*

Hitczenko, M. and Stein, M. L. (2012). Some theory for anisotropic processes on the sphere. *Statistical Methodology* **9**, 211–227.

Isaaks, E. H. and Srivastava, R. M. (2001). An Introduction to Applied Geostatistics. 1989. New York, USA: *Oxford University Press. Jones DR, A Taxonomy of Global Optimization Methods Based on Response Surfaces. Journal of Global Optimization* **23**, 345–383.

Johnstone, I. M. (2001). On the distribution of the largest eigenvalue in principal components analysis. *The Annals of Statistics*, 295–327.

Jones, R. H. (1963). Stochastic processes on a sphere. *The Annals of Mathematical Statistics* **34**, 213–218.

Jun, M. and Genton, M. G. (2012). A test for stationarity of spatio-temporal random fields on planar and spherical domains. *Statistica Sinica* **22**, 1737–1764.

Li, B., Genton, M. G. and Sherman, M. (2007). A nonparametric assessment of properties of space–time covariance functions. *Journal of the American Statistical Association* **102**, 736–744.

Li, B., Genton, M. G. and Sherman, M. (2008). On the asymptotic joint distribution of sample space-time covariance estimators. *Bernoulli* **14**, 228–248.

Lu, H. and Zimmerman, D. L. (2001). Testing for isotropy and other directional symmetry properties of spatial correlation preprint

Maity, A. and Sherman, M. (2012). Testing for spatial isotropy under general designs. *Journal of Statistical Planning and Inference* **142**, 1081–1091.

Matheron, G. (1961). Precision of exploring a stratified formation by boreholes with rigid spacing-application to a bauxite deposit. *International Symposium of Mining Research, University of Missouri* **1**, 407–422.

Matsuda, Y. and Yajima, Y. (2009). Fourier analysis of irregularly spaced data on Rd. *Journal of the Royal Statistical Society: Series B (Statistical Methodology)* **71**, 191–217.

Misra, V. (2004). The teleconnection between the western Indian and the western Pacific Oceans. *Monthly Weather Review* **132**, 445–455.

Reason, C. J. C. and Mulenga, H. (1999). Relationships between South African rainfall and SST anomalies in the southwest Indian Ocean. *International Journal of Climatology* **19**, 1651–1673.

Schramm, P. J., Uejio, C. K., Hess, J. J., Marinucci, G. D. and Luber, G(2014). Climate models and the use of climate projections. *National Center for Environmental Health, Centers for Disease Control and Prevention*

Stein, M. L. (2005). Statistical methods for regular monitoring data. *Journal of the Royal Statistical Society: Series B (Statistical Methodology)* **67**, 667–687.

127 Manchester Hall, Box 7388, Winston Salem, NC 27109, USA.

E-mail: sahooi@wfu.edu

1178 Comstock Hall, Ithaca, NY 14853,USA.

E-mail: guinness@cornell.edu

Campus Box 8203, 5212 SAS Hall, Raleigh, NC 27965,USA.

E-mail: bjreich@ncsu.edu

(Received November 2017; accepted November 2018)